



Subcritical Hopf and saddle-node bifurcations in hunting motion caused by cubic and quintic nonlinearities: experimental identification of nonlinearities in a roller rig

Weiyan Wei · H. Yabuno

Received: 9 October 2018 / Accepted: 24 August 2019 / Published online: 4 September 2019
© Springer Nature B.V. 2019

Abstract Railway vehicles suffer from hunting motion, even when traveling below the critical speed obtained by linear analysis, due to the nonlinear characteristics of the wheel system. Nonlinear characteristics in Hopf bifurcations can be characterized as subcritical or supercritical, depending on whether the cubic nonlinearity is softening or hardening, respectively. In a system with softening cubic nonlinearity, third-order nonlinear analysis cannot detect nontrivial stable steady-state oscillations because they are affected by quintic nonlinearity. Therefore, in such a system, it is necessary to apply fifth-order nonlinear analysis to a system model in which quintic nonlinearity is taken into account. In this study, we investigated the cubic and quintic nonlinear phenomena in hunting motion with a roller rig that is widely used for hunting motion research. Previous experimental studies using a roller rig were restricted to the linear stability and the cubic nonlinear stability. We clarified that roller rig experiments can observe the hysteresis phenomenon and the existence of subcritical Hopf and saddle-node bifurcations, indicating that not only the cubic but also the quintic nonlinearity of the wheel system plays an important role. In addition, we obtained the normal form governing the nonlinear dynamics. We developed

an experimental identification method to obtain the coefficients of the normal form. The validity of our method was confirmed by comparing the bifurcation diagrams obtained from the experimental time history and the normal form whose coefficients were experimentally identified using the proposed method.

Keywords Hunting motion · Roller rig · Quintic nonlinearity · Subcritical Hopf bifurcation · Saddle-node bifurcation · Hysteresis · Experimental identification of nonlinear parameters

1 Introduction

Vehicle stability is one of most important railway design criteria [1] because instability is directly related to the reduction in ride comfort, damage to the wheels, and risk of derailment. More attention has recently been paid to the development of high-speed railways. The key problems of high-speed vehicles can be summarized as the train-track coupling, the interaction of wheel and rail, and noise from vibration [2]. Researchers have contributed to the solution of these problems from a variety of perspectives. For example, the undesirable effects due to increased dynamic response of the wheel system have been investigated by accounting for the hanging sleepers under the rail [3]. In addition, the effects of the wheel flat length were studied to guide the maintenance of wheel-rail components in railway systems [4].

W. Wei (✉) · H. Yabuno
Graduate School of Systems and Information Engineering,
University of Tsukuba, Tsukuba, Ibaraki, Japan
e-mail: 455066951wwy@gmail.com

H. Yabuno
e-mail: yabuno@esys.tsukuba.ac.jp

Among these problems, a self-excited oscillation, called hunting motion, is produced when the running speed exceeds a critical value [5]. This critical speed is usually obtained from a linear eigenvalue analysis and is specifically called the linear critical speed. The hunting motion is a kind of fluttering, self-excited oscillation due to the contact force between the wheels and the track, which is called creep force [6]. In this paper, we focus on this particular phenomenon in wheel systems.

Wickens investigated the influence of various parameters on the stability of railway vehicles by linear analysis with full-scale and simplified models [7,8]. Suitable choices of the suspension and other parameters to increase the linear critical speed of hunting motion were posited, and their validity was verified by experiments. Doyle and Prause investigated the effects of torsionally flexible wheelsets on the hunting stability of rail vehicles [9]. Lee and Cheng derived the governing differential equations of motion for a truck moving on tangent tracks using the linear creep model [10]. Chi et al. studied the influence of bogie hunting motion on ride quality of railway vehicles in the frequency domain by calculating the hunting mode of the bogie and the natural mode of the car body [11]. Baldovin et al. proposed a stability method for hunting motion with linear dissipation devices [12]. However, recent investigations indicated that the nonlinear characteristics of hunting motion are caused by the inherent nonlinearities of railway vehicle systems. Hopf bifurcation is produced at the linear critical speed point and if it is subcritical, hunting motion will be produced even below the linear critical speed, depending on the magnitude of the disturbance [13–15]. Existing studies on nonlinearity in the system have pointed to nonlinear causes, such as flange contact, gauge clearance, and nonlinear rail/wheel geometry [16–18]. One of the most effective nonlinear forces acting on the wheel is the contact force, which is expressed by a nonlinear creep force, such as that described by Chartet's formulation [19], Kalker's formulation [16], and Wagner's function [20].

In general, it is well known that Hopf bifurcation can be produced by the cubic nonlinearity of a system. There are two types of nonlinear characteristics, supercritical and subcritical [21]. The hunting motion exhibits supercritical or subcritical Hopf bifurcation when the cubic nonlinearity is hardening or softening, respectively. These bifurcation modes show qualitatively different characteristics near the linear critical speed. During subcritical Hopf bifurcation, there is

an unstable nontrivial saddle, that is, an unstable limit cycle, below the linear critical speed. Even below the critical speed, hunting motion begins if the magnitude of disturbance is larger than the unstable limit cycle. However, in the case of supercritical Hopf bifurcation, there is a stable nontrivial steady state, which corresponds to a stable limit cycle above the linear critical speed. When the running speed is gradually increased from the linear critical speed, the amplitude of the vehicle continuously changes from zero.

To investigate these nonlinear behaviors for railway vehicles, a bifurcation diagram around the critical speed is obtained by numerical simulations [22–29] and experiments [13,30,31]. In addition, recent research [32] clarified that differences in bogie parameters determine whether the nonlinear characteristic of Hopf bifurcation is supercritical or subcritical. Chi et al. [31] claimed that increasing the longitudinal stiffness of the primary suspension transforms the subcritical Hopf bifurcation to a supercritical one. The Chinese high-speed railway vehicles of types CRH2 and CRH3 exhibit subcritical and supercritical Hopf bifurcations, respectively [33]. These differences in the bifurcation are caused by the differences in matching relations between bogie parameters and wheel profiles.

As a fundamental experimental device to study the vehicle stability, a roller rig for realistic vehicles or simplified modes has been used for researching Shinkansen bullet trains in Japan since the 1950s [34] because of its advantages for studying wheel system parameters. Ejiri et al. [35] experimentally analyzed the running stability of an independently rotating wheel set using a scale-model roller rig. The results showed the same hunting characteristics as those seen in numerical simulation. Furthermore, Myamlin et al. [36] studied the possibilities of various roller rigs for stability experiments.

The application of roller rigs to detect the linear characteristics of hunting motion has become widespread in recent decades [37]. However, few experimental studies have used roller rigs to investigate the nonlinear characteristics of hunting motion. Previous experimental studies are restricted to cubic nonlinearity [13] and do not mention the effects of quintic nonlinearity in vehicles. Yamanaga et al. investigated the global stability of hunting motion using a real bogie [38]. The connected unstable nontrivial steady state and stable nontrivial steady state in the experimental results verified the existence of the saddle-node bifurcation phenomenon. They concluded that a suitable additional

force can be used to stabilize the hunting oscillation when the running speed is smaller than the linear critical speed. However, they did not theoretically analyze a bogie model.

In this paper, we describe the study of hunting motion due to cubic and quintic nonlinearities with a roller rig. Nonlinear hunting motion with subcritical Hopf and saddle-node bifurcations was experimentally observed, where a stable trivial steady state and a stable limit cycle coexist below the linear critical speed. Hence, the hysteresis of a single wheel set was observed in our experiment. This result suggests that the roller rig experimental method can be extended to the investigation of nonlinear phenomena in wheel systems, including cubic and quintic nonlinear phenomena.

Then, we examine the normal form [39] to show the nonlinear characteristics of hunting motion and propose an experimental identification method for the four essential coefficients included in the normal form with the aid of center manifold theory. Nonlinear phenomena based on quintic nonlinearity are often observed in actual systems [40], as well as in experiments with roller rigs. The identification of coefficients included in the normal form is necessary to theoretically obtain the bifurcation diagram. By comparing the bifurcation diagram theoretically obtained using the values of the experimentally identified coefficients and the bifurcation diagram directly obtained from experimental data, we clarify the validity of the proposed experimental identification method for the four coefficients in the normal form.

2 Experimental observation of bifurcations in hunting motion due to quintic nonlinearity

2.1 Wheel set and roller rig

The roller rig and single wheel set used in this study are shown in Fig. 1, and the experimental setup is shown in Fig. 2. We placed the wheel set, which could freely move in the lateral and yaw directions, on the roller rig to simulate the running of a railway vehicle in a straight line. The roller rig is rotated by an AC motor (Miki Pulley Corp., SEM-400B), and various rotational speeds can be set using a speed controller. The running speed of the wheel set is measured by an encoder (Fuji Instrument Manufacturing Corp., PG-10800) and displayed on a speed meter (Omron Corp., K3M R-

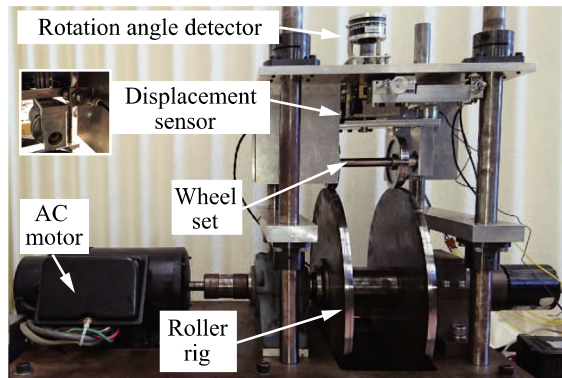


Fig. 1 Photo of wheel set and roller rig

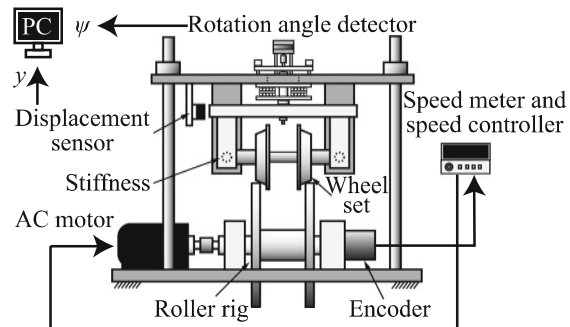


Fig. 2 Experimental setup

NB1A-B2) in real time. The analog signals of the lateral displacement y and yaw angle ψ are measured by a non-contact displacement sensor (Emic Corp., 503-F) and a rotation angle detector (MinebeaMitsumi Corp., DM-40A), respectively. As shown in Fig. 2, the analog signal is sent to a PC and translated into a time history and power spectrum diagram.

2.2 Cubic and quintic nonlinearities in the wheel system

By the analytical model considering only cubic nonlinearity in addition to the linear component in the external force and moment, it is theoretically shown that the bifurcation of supercritical or subcritical Hopf bifurcation occurs. In the case of the subcritical Hopf bifurcation, as shown in Fig. 3, we cannot find the nontrivial stable steady-state amplitude above the linear critical speed [13].

The subcritical Hopf bifurcation diagram under the effects of cubic and quintic nonlinearities was obtained

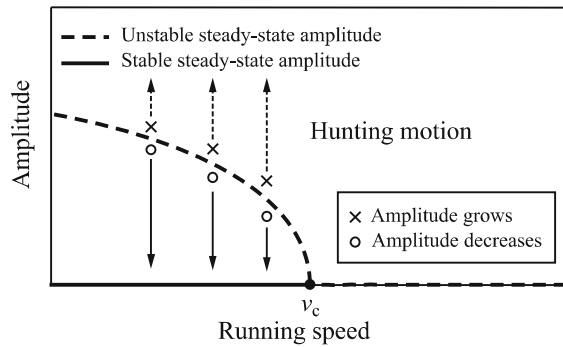


Fig. 3 Schematic diagram of subcritical Hopf bifurcation under the effect of cubic nonlinearity [13]

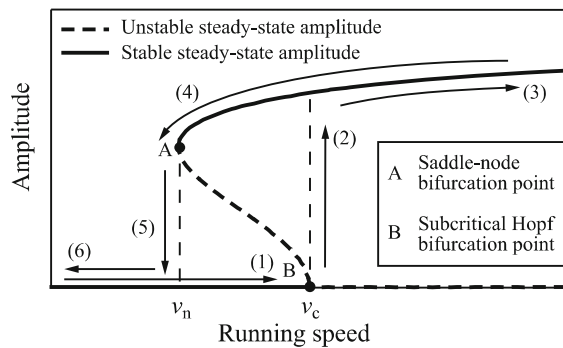


Fig. 4 Bifurcation diagram obtained by numerical simulation for the model considering the effects of cubic and quintic nonlinearities [30,41]. The numbered arrows correspond to those in Fig. 6

by numerical simulations [30,41], as shown in Fig. 4. The unstable nontrivial steady state that appears at the linear critical speed (point B) is due to cubic nonlinearity. The stable nontrivial steady state that appears at point A is due to quintic nonlinearity. When the running speed approaches point A, the two steady-state amplitudes cancel each other out. This point is the so-called saddle-node bifurcation point, which does not exist in an analytical model that considers only cubic nonlinearity, as shown in Fig. 3.

2.3 Experimental observation of linear and nonlinear critical speeds

The time histories of lateral and yaw directions of the wheel set were recorded at different running speeds, and the data in the steady state were translated into a spectrum diagram. The running speed of the wheel set was increased or decreased slowly to prevent artificial

noise. Under fluctuation noise, such as that caused by roughness of the surface of the roller rig and wheels, the critical speed obtained from the experiments corresponded to that obtained by the linear theory.

To observe the saddle-node bifurcation, we focused on another critical running speed, which is at the saddle-node point and called the nonlinear critical speed (v_n). Below this running speed, the hunting motion does not appear independently of the magnitude of disturbance. In such a wheel system, the stable steady-state amplitude during decreasing running speed is different from the stable steady-state amplitude during increasing running speed. This nonlinear phenomenon is called hysteresis [42,43], and it is widely observed in engineering systems.

To evaluate this feature, we first increased the running speed to obtain the linear critical speed (v_c), where the hunting motion appears, as shown by the arrow labeled (2). Furthermore, we continuously increased the running speed to observe the dependency of steady-state amplitude on the running speed. After that, we decreased the running speed. The hunting motion disappears when the running speed reaches point A, that is, the nonlinear critical speed.

2.4 Experimental results

The time histories, power spectrum, phase portrait, Poincaré section, and Lyapunov values of the steady-state lateral displacement at different running speeds are shown in Fig. 5. We focused on the lateral displacement because the result of yaw angle is similar to that of the lateral displacement. As shown in Fig. 5, the amplitude of the oscillation was not constant according to the additional frequency component due to the roughness of the surface of the roller rig and wheels. In this case of fluctuation noise, the component of hunting motion in the power spectrum diagram varies with time. Therefore, we cannot directly use this component in the power spectrum to express the steady-state amplitude of hunting motion. In this situation, we regard the average value of the maximum amplitude of the oscillation in the time history as the steady-state amplitude. The resulting experimentally obtained steady-state amplitudes of the lateral displacement y_{amp} are shown in Fig. 6. The circles and crosses in the figure denote the steady-state amplitude at increasing and decreasing running speeds, respectively. The linear critical speed

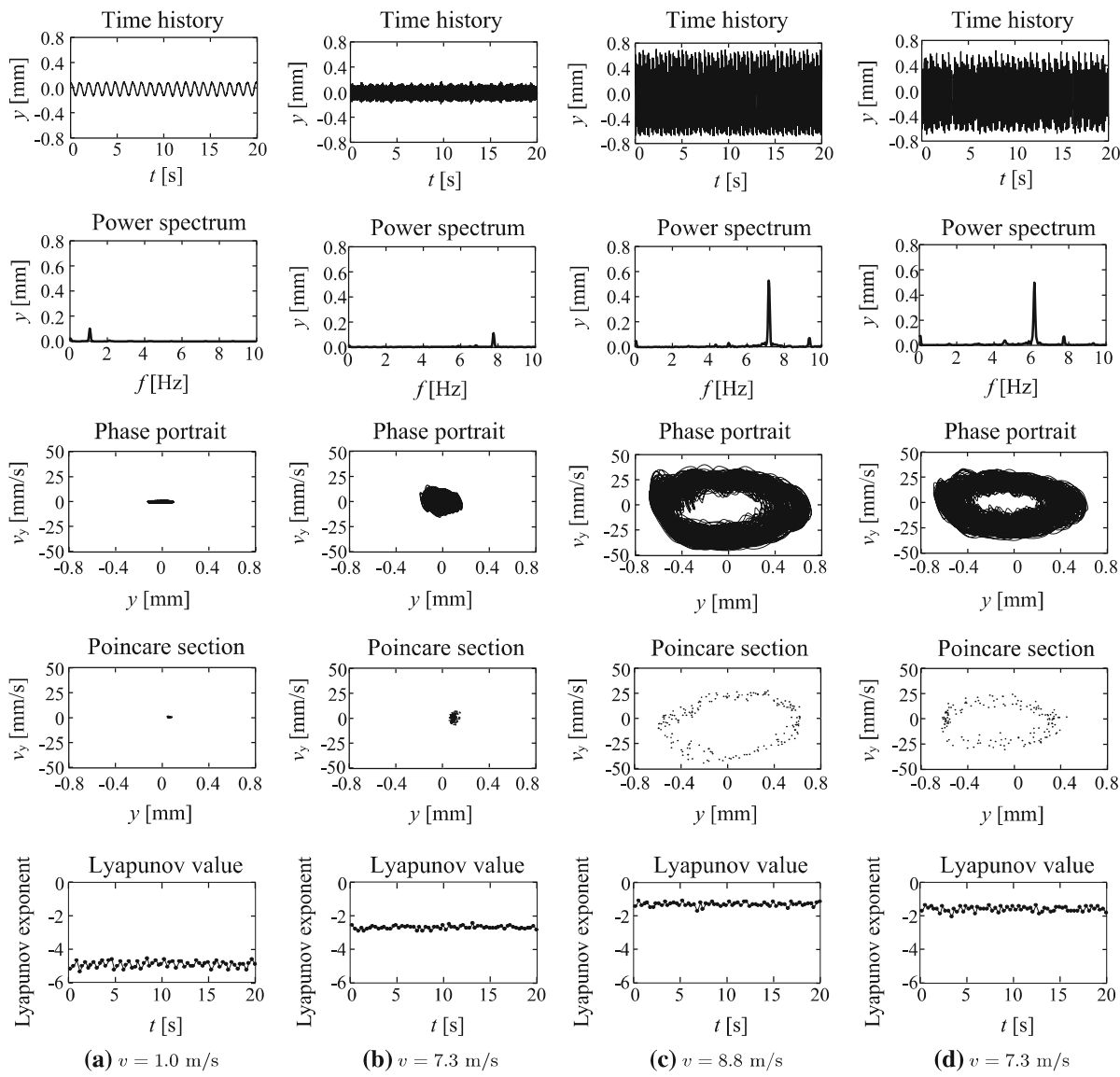


Fig. 5 Time history, power spectrum, phase portrait, Poincare section, and Lyapunov values of the steady-state lateral displacement at different running speeds. Panels **a**, **b** and **c** are observa-

tions for increasing running speed. Panel **d** is observation for decreasing running speed

of hunting motion is 8.0 m/s (29 km/h), as in Fig. 6, where the amplitude of oscillation grows quickly to a larger steady-state amplitude.

We discuss representative time histories in the order of the numbered arrows in Fig. 6. When the running speed is less than the linear critical speed, the lateral oscillation has a small amplitude, as in Fig. 5a, b. Here, the amplitude is not 0 because of the fluctuation noise due to the roughness of the roller rig and wheels. In other words, the roughness creates the observed spec-

trum. The frequency of the roughness component ω_r can be expressed as follows:

$$\omega_r = \frac{v}{D\pi} \approx 1.06v, \quad (1)$$

where v is the running speed of the wheel set and D is the diameter of the roller rig (0.3 m). Figure 5 shows the hunting motion. There are two spectra in this time history; the upper spectrum is due to the periodic

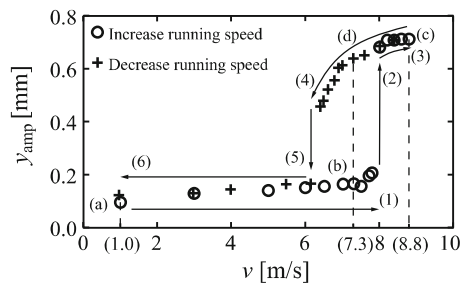


Fig. 6 Experimentally observed steady-state amplitude of lateral displacement. The numbered arrows correspond to those in Fig. 4. The points labeled **a–d** correspond to the panels of Fig. 5

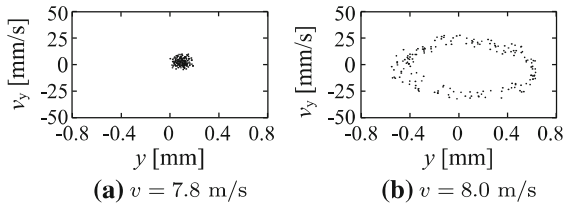


Fig. 7 Variation of Poincare maps below and above the linear critical speed

roughness fluctuation, and the lower spectrum is due to the hunting motion. The roughness also affects the linear and nonlinear critical speeds. Further discussion of this is given in “Appendix A.” We did not explore the speed zone above 9 m/s (32 km/h) because the steady-state amplitude of wheel set almost reaches a maximum amplitude due to the flange limit at point (c). After that, we decreased the running speed. Even below the linear critical speed, the resonance persists because the amplitude is larger than the unstable steady-state branch due to the subcritical Hopf bifurcation, as in Fig. 5d. The difference of steady-state amplitude between Fig. 5b, d is due to the hunting motion. The nonlinear speed of hunting motion is about 6.0 m/s (21 km/h), as in Fig. 6.

In Fig. 5, the Poincare sections of (a) and (b) show a periodic orbit, and the Poincare sections of (c) and (d) show a quasi-periodic orbit. Moreover, in Fig. 7a, b, we illustrate two running speeds near the linear critical speed of hunting motion, where the minimum interval of running speed is about 0.2 m/s due to the accuracy of our experimental device. This figure shows that a periodic orbit becomes a quasi-periodic orbit as the running speed increases. Therefore, in our experiment, the period-doubling bifurcation phenomenon was not detected. In addition, the negative Lyapunov exponents indicate that the experimental oscillation of the single wheel set is nonchaotic.

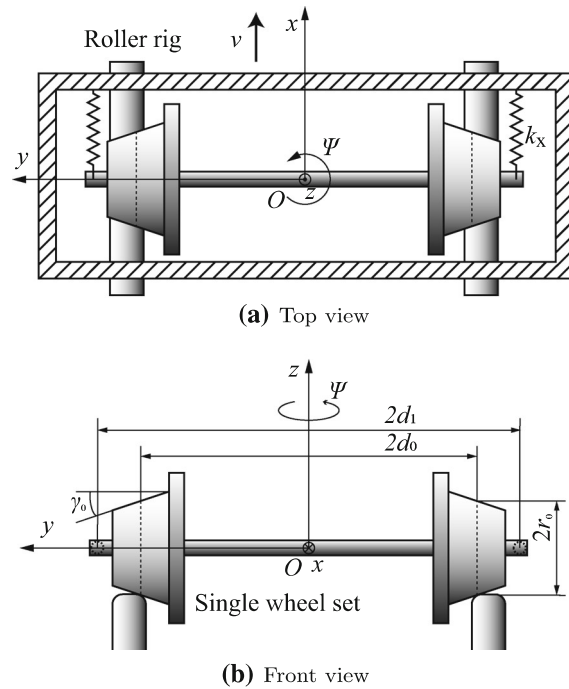


Fig. 8 Configuration of the single wheel set and roller rig

In conclusion, the subcritical Hopf and saddle-node bifurcations were experimentally observed using the roller rig. To investigate such phenomena theoretically, it is necessary to account for the quintic nonlinearity in the system by performing fifth-order nonlinear analysis.

In the next section, we present a simplified equation for nonlinear hunting motion, that is a normal form, with the aid of center manifold theory and propose a method for identifying the coefficients of the normal form from the experimental results in this section.

3 Normal form of quintic nonlinear hunting motion and experimental identification of the nonlinearity

3.1 Equation of motion

First, we consider a mathematical model of a suspended single wheel set with two degrees of freedom, lateral motion y and yaw motion ψ , as shown in Fig. 8, which has been commonly used as an essential model [44–46]. In the figure, r_0 is the centered wheel rolling radius, k_x is the x direction stiffness, γ_0 is the wheel tread angle,

Table 1 Parameters of the experimental setup

Description	Symbol	Value	Unit
Mass of the wheel set	m	2.175	kg
Half-track gauge	d_0	0.0485	m
Half-gap of stiffness	d_1	0.085	m
Centered wheel rolling radius	r_0	0.036	m
Equilibrium state spring length	l	0.06	m
Natural spring length	l_0	0.035	m
Wheel tread angle	γ_0	1/25	—
x Direction stiffness	k_x	200	N/m
Moment of inertia	I	0.0043	kg m^2
Lateral natural frequency	ω_y	8.754	rad/s
Yaw natural frequency	ω_ψ	25.91	rad/s

d_0 is the half-track gauge, x is the running direction, and v is the running speed. The parameter values corresponding to the experimental apparatus used in this study are shown in Table 1.

We used the half-track gauge d_0 as the representative length and the inverse value of the linear natural frequency of yaw motion ω_ψ as the representative time to obtain the dimensionless equations governing the dimensionless lateral and yaw motions y^* and ψ , respectively, as in [6, 13]:

$$\ddot{y}^* + \frac{d_{11}}{v^*} \dot{y}^* + k_{11}y^* + k_{12}\psi + \alpha_{30}y^{*3} + \alpha_{21}y^{*2}\psi + \dots + \alpha_{03}\psi^3 + \alpha_{50}y^{*5} + \alpha_{41}y^{*4}\psi + \alpha_{32}y^{*3}\psi^2 + \dots + \alpha_{05}\psi^5 = 0, \quad (2)$$

$$\ddot{\psi} + \frac{d_{22}}{v^*} \dot{\psi} + k_{21}y^* + k_{22}\psi + \beta_{30}y^{*3} + \beta_{21}y^{*2}\psi + \dots + \beta_{03}\psi^3 + \beta_{50}y^{*5} + \beta_{41}y^{*4}\psi + \beta_{32}y^{*3}\psi^2 + \dots + \beta_{05}\psi^5 = 0, \quad (3)$$

where dots denote the derivative with respect to the dimensionless time t^* and v^* denotes the dimensionless running speed. The dimensionless coefficients of the above equations are expressed by the dimensional parameters as follows:

$$d_{11} = \frac{2\kappa_{yy}}{md_0\omega_\psi^2}, \quad d_{22} = \frac{\kappa_{xx}d_0}{k_x d_1^2}, \quad k_{11} = \frac{\omega_y^2}{\omega_\psi^2}, \quad v^* = \frac{v}{d_0\omega_\psi},$$

$$k_{12} = \frac{-2\kappa_{yy}}{md_0\omega_\psi^2}, \quad k_{21} = \frac{d_0^2\kappa_{xx}\gamma_0}{k_x d_1^2 r_0}, \quad k_{22} = 1, \quad (4)$$

where κ_{xx} and κ_{yy} are creep coefficients in the x and y directions, respectively [31, 33]; $\alpha_{30}y^{*3}, \dots, \beta_{03}\psi^3$ are cubic nonlinear terms with 8 unknown coefficients $\alpha_{30}, \dots, \beta_{03}$; and $\alpha_{50}y^{*5}, \dots, \beta_{05}\psi^5$ are quintic nonlinear terms with 12 unknown coefficients $\alpha_{50}, \dots, \beta_{05}$. In general, the coefficients of 8 cubic and 12 quintic nonlinear terms are governed by the nonlinearity of the suspension and contact force. According to previous studies, the source of nonlinear forces acting on the wheel can include the flange contact, gauge clearance, and rail/wheel geometry [13–15]. These nonlinear effects can usually be considered as symmetric nonlinear terms and are approximated by the odd power series with respect to displacement and rotation angle of the wheel set. The nonlinear terms in Eqs. (2) and (3) comprehensively represent these nonlinear effects to analytically solve the equations of motion. In typical lowest-order consideration of symmetric nonlinearities, only the cubic nonlinearity is taken into account in the equations of motion. However, the necessity of higher-order nonlinearity is indicated here to clarify the nonlinear hunting motion in this study. Therefore, quintic nonlinearity is also considered in the equations of motion. In this section, we derive a normal form to express the quintic nonlinear hunting motion that was experimentally observed in Sect. 2 and clarify the least nonlinear terms theoretically to show the nonlinear phenomenon. Furthermore, we propose a method to experimentally identify the coefficients of the nonlinear terms.

3.2 Normal form

3.2.1 Reduction in the dimensionality using center manifold theory

We investigate the quintic nonlinear characteristics of hunting motion around the linear critical speed. First, we use a small parameter ϵ ($|\epsilon| \ll 1$) to express the dimensionless running speed as follows:

$$v^* = v_c^*(1 + \epsilon), \quad (5)$$

where v_c^* denotes the dimensionless linear critical speed of hunting motion. Therefore, the dimensionless equations of motion, Eqs. (2) and (3), are rewritten in matrix form as follows:

$$\dot{x} = Ax + N(x, \epsilon), \quad (6)$$

where

$$\mathbf{x} = \begin{bmatrix} y^* \\ \dot{y}^* \\ \psi \\ \dot{\psi} \end{bmatrix}. \quad (7)$$

According to the calculation in ‘‘Appendix B,’’ Eq. (6) can be transformed to a real Jordan form using a transformation matrix \mathbf{P} as

$$\dot{\mathbf{z}} = \begin{bmatrix} 0 & \omega & 0 & 0 \\ -\omega & 0 & 0 & 0 \\ 0 & 0 & \lambda_R & \lambda_I \\ 0 & 0 & -\lambda_I & \lambda_R \end{bmatrix} \mathbf{z} + N'(\mathbf{z}, \epsilon), \quad (8)$$

where

$$\mathbf{z} = \begin{bmatrix} z_1 \\ z_2 \\ z_3 \\ z_4 \end{bmatrix}, \quad (9)$$

and

$$\mathbf{z} = \mathbf{P}^{-1} \mathbf{x}. \quad (10)$$

The reduction in the dimensionality of Eq. (8) can be carried out using the center manifold theory for the case in which a pair of pure imaginary eigenvalues, and one complex conjugate pair of eigenvalues with a negative real part exists in the dynamical system [13, 47].

By balancing the detuning terms $\epsilon z_1, \epsilon z_2$ and cubic nonlinear terms $z_1^3, z_1^2 z_2, \dots, z_2^3$ with the detuning terms $\epsilon^2 z_1, \epsilon^2 z_2, \epsilon z_1^3, \epsilon z_1^2 z_2, \dots, \epsilon z_2^3$ and the quintic nonlinear terms $z_1^5, z_1^4 z_2, \dots, z_2^5$, we can estimate z_1 and z_2 as $O(\epsilon^{1/2})$. Therefore, the orders of cubic and quintic nonlinear terms are $O(\epsilon^{3/2})$ and $O(\epsilon^{5/2})$, respectively. Then, the center manifold is expressed by $z_3 = h_3(\epsilon, z_1, z_2) = O(\epsilon^{5/2})$ and $z_4 = h_4(\epsilon, z_1, z_2) = O(\epsilon^{5/2})$. Hence, z_3 and z_4 can be expressed as follows:

$$\begin{aligned} z_3 &= D_{3110}\epsilon z_1 + D_{3101}\epsilon z_2 + D_{3030}z_1^3 + D_{3021}z_1^2 z_2 \\ &\quad + D_{3012}z_1 z_2^2 + D_{3003}z_2^3 + D_{3210}\epsilon^2 z_1 + D_{3201}\epsilon^2 z_2 \\ &\quad + D_{3130}\epsilon z_1^3 + D_{3121}\epsilon z_1^2 z_2 + D_{3112}\epsilon z_1 z_2^2 + D_{3103}\epsilon z_2^3 \\ &\quad + D_{3050}z_2^5 + D_{3041}z_1^4 z_2 + D_{3032}z_1^3 z_2^2 + D_{3023}z_1^2 z_2^3 \\ &\quad + D_{3014}z_1 z_2^4 + D_{3005}z_2^5, \end{aligned} \quad (11)$$

$$z_4 = D_{4110}\epsilon z_1 + D_{4101}\epsilon z_2 + \dots + D_{4005}z_2^5. \quad (12)$$

According to the standard strategy, we determine the dynamics on the center manifold [48]. Substituting Eq. (11) and the first and second rows of Eq. (8) into

$$\dot{z}_3 = \frac{\partial z_3}{\partial z_1} z_1 + \frac{\partial z_3}{\partial z_2} z_2, \quad (13)$$

yields \dot{z}_3 , which is also expressed in the third row of Eq. (8):

$$\dot{z}_3 = \lambda_R z_3 + \lambda_I z_4 + N'_3(z, \epsilon). \quad (14)$$

Equating Eqs. (13) and (14) yields the coefficients of $D_{3110}, \dots, D_{3005}$. In addition, the equations with respect to z_4 can also be obtained. Therefore, we can have 36 equations for 36 unknown coefficients of $D_{3110}, \dots, D_{4005}$. Then, all the coefficients are obtained and the center manifold is determined with Eqs. (11) and (12). Moreover, substituting these equations into the first and the second rows of Eq. (8) gives us the equations governing the dynamics in the center manifold as

$$\begin{bmatrix} \dot{z}_1 \\ \dot{z}_2 \end{bmatrix} = \begin{bmatrix} 0 & \omega \\ -\omega & 0 \end{bmatrix} \begin{bmatrix} z_1 \\ z_2 \end{bmatrix} + N''(z_1, z_2, \epsilon). \quad (15)$$

Moreover, by using a transformation matrix \mathbf{P}' , the coordinate (z_1, z_2) is changed into a complex coordinate ζ , and Eq. (15) is transformed into

$$\begin{bmatrix} \dot{\zeta} \\ \ddot{\zeta} \end{bmatrix} = \begin{bmatrix} i\omega & 0 \\ 0 & -i\omega \end{bmatrix} \begin{bmatrix} \zeta \\ \bar{\zeta} \end{bmatrix} + N'''(\zeta, \bar{\zeta}, \epsilon), \quad (16)$$

where we can only focus on the first row, and the conversion relationship is expressed as follows:

$$\begin{bmatrix} \zeta \\ \bar{\zeta} \end{bmatrix} = \mathbf{P}'^{-1} \begin{bmatrix} z_1 \\ z_2 \end{bmatrix}, \quad (17)$$

where

$$\mathbf{P}'^{-1} = \frac{1}{2} \begin{bmatrix} 1 & -i \\ 1 & i \end{bmatrix}. \quad (18)$$

3.2.2 Normal form for quintic nonlinear hunting motion

First, we introduce the nonlinear transformation

$$\zeta = \eta + q(\eta, \bar{\eta}, \epsilon), \quad (19)$$

where $q(\eta, \bar{\eta}, \epsilon)$ is a nonlinear function that is expressed by 6 cubic and 12 quintic nonlinear terms with 18 selectable coefficients as follows:

$$\begin{aligned} q(\eta, \bar{\eta}, \epsilon) = & \Gamma_1 \epsilon \eta + \Gamma_2 \epsilon \bar{\eta} + \Gamma_3 \eta^3 + \cdots + \Gamma_7 \epsilon^2 \eta \\ & + \Gamma_8 \epsilon^2 \bar{\eta} + \Gamma_9 \eta^5 + \cdots + \Gamma_{18} \bar{\eta}^5. \end{aligned} \quad (20)$$

These coefficients are selected so as to reduce the number of nonlinear terms included in the equation transformed by Eq. (19). Substitution of Eq. (19) into Eq. (16) gives us the following equation:

$$\dot{\eta} + \frac{\partial q}{\partial \eta} \dot{\eta} + \frac{\partial q}{\partial \bar{\eta}} \dot{\bar{\eta}} = i\omega \eta + i\omega q + \hat{N}_1(\eta, \bar{\eta}, \epsilon). \quad (21)$$

Through the calculation described in “Appendix C,” by which suitable coefficients were selected for Eq. (20), we obtain the simplified equation of η as follows:

$$\dot{\eta} = i\omega \eta + D_1 \epsilon \eta + D_4 \eta^2 \bar{\eta} + \Gamma'_7 \epsilon^2 \eta + \Gamma'_{10} \epsilon^2 \bar{\eta} + \Gamma'_{15} \eta^3 \bar{\eta}^2. \quad (22)$$

By substituting

$$\eta = r e^{i\theta} \quad (23)$$

into Eq. (22), we obtain the real and imaginary parts as follows:

Real:

$$\dot{r} = D_{1R} \epsilon r + D_{4R} r^3 + D'_{7R} \epsilon^2 r + D'_{10R} \epsilon r^3 + D'_{15R} r^5, \quad (24)$$

Imaginary:

$$\dot{\theta} = \omega + D_{1I} \epsilon + D_{4I} r^2 + D'_{7I} \epsilon^2 + D'_{10I} \epsilon r^2 + D'_{15I} r^4, \quad (25)$$

where D_{jR} and D_{jI} are the real and imaginary parts of D_j , respectively. The normal form of the wheel sys-

tem is obtained as Eq. (24), where the linear coefficient $D_{1R}\epsilon$ can be expressed by the dimensionless speed v_{cr}^* and dimensionless linear parameters $d_{11}, d_{22}, k_{11}, \dots, k_{22}$ in the governing equations, (2) and (3) (in the preceding experiment, $D_{1R}\epsilon = 0.12\epsilon$). The coefficient $D'_{7R}\epsilon^2$ is not affected by the linear terms in the original equations. The coefficients of the cubic nonlinear terms D_{4R} , $D'_{10R}\epsilon$ and the coefficients of the quintic nonlinear terms D'_{15R} are related to the linear parameters and the 20 coefficients of the nonlinear terms in Eqs. (2) and (3). However, not all parameters in these equations are needed to describe the quintic nonlinear hunting motion; rather, it is sufficient to know the four unknown coefficients in the normal form D_{1R} , D_{4R} , D'_{10R} , and D'_{15R} . In the next section, we propose an experimental method to obtain these parameter values.

3.3 Experimental identification of nonlinear coefficients in the normal form

Setting $\dot{r} = 0$ yields the equilibrium equation

$$r_{st}[D_{1R}\epsilon + D_{4R}r_{st}^2 + D'_{7R}\epsilon^2 + D'_{10R}\epsilon r_{st}^2 + D'_{15R}r_{st}^4] = 0. \quad (26)$$

From Eq. (26), there is a trivial steady state

$$r_{st} = 0, \quad (27)$$

and a nontrivial steady state that satisfies

$$D_{1R}\epsilon + D_{4R}r_{st}^2 + D'_{7R}\epsilon^2 + D'_{10R}\epsilon r_{st}^2 + D'_{15R}r_{st}^4 = 0. \quad (28)$$

According to the nonlinear transformation Eq. (19) and polar form Eq. (23), we can have

$$\zeta \approx \eta = r e^{i\theta}. \quad (29)$$

In addition, by substituting the conversion relationship Eq. (17), we express z_1 as

$$z_1 = \zeta + \bar{\zeta} = 2r. \quad (30)$$

Moreover, according to the transformation Eq. (10) and the center manifold theory, we can express the relationship as follows:

$$y^* = x_1 = z_1 + z_3 \approx z_1. \quad (31)$$

Therefore, the relationship between dimensionless r_{st} and dimensional y_{amp} in millimeters can be expressed as

$$y_{amp} = 2d_0 r_{st} = 0.097 r_{st}. \quad (32)$$

We experimentally identify the four coefficients using four stable amplitudes of the experimental results at the four different running speeds $\epsilon_1 = -0.2$, $\epsilon_2 = -0.1$, $\epsilon_3 = 0$, and $\epsilon_4 = 0.1$. These correspond to the dimensional running speeds $v_1 = 6.4$ m/s, $v_2 = 7.2$ m/s, $v_3 = 8.0$ m/s, and $v_4 = 8.8$ m/s, respectively. Here, v_1 is the nonlinear critical speed at which hunting motion disappears, v_3 is the linear critical speed at which hunting motion occurs, v_2 is the speed at the midpoint between v_1 and v_3 , and v_4 is a speed greater than the speed v_3 . Then, from Eq. (28), we identify the coefficients as

$$\begin{aligned} D_{4R} &= 2030, D'_{7R} = -0.06, \\ D'_{10R} &= -360, D'_{15R} = -4.2 \times 10^7. \end{aligned} \quad (33)$$

As a result, we can use Eq. (24) to obtain the theoretical bifurcation diagram corresponding to the experimental roller rig system as Fig. 9, where the solid and dashed curves are stable and unstable steady states, respectively. The amplitude changes from point (a-1) to point (a-4) through points (b-3), (a-2), and (a-3) as the running speed increases. The amplitude changes from point (b-1) to point (a-1) as the running speed decreases. Moreover, points (a-2) and (b-2) are the Hopf bifurcation and saddle-node bifurcation points, respectively, which correspond to the linear and nonlinear critical speeds.

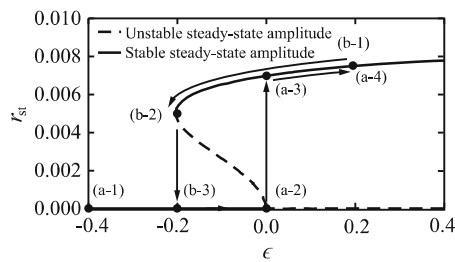


Fig. 9 Theoretically obtained saddle amplitude of r for the experimental system. The alphanumerically identified points are discussed in the text

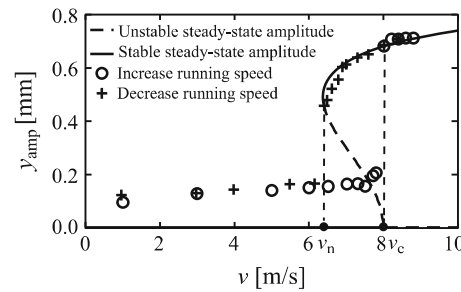


Fig. 10 Comparison of theoretical and experimental results for steady-state amplitude of lateral displacement of the single wheel set

Finally, we obtain the theoretical steady-state amplitude diagram of the lateral displacement. To confirm the validity of the experimental identification method, we compared the bifurcation diagrams obtained by the experimental time history and the normal form whose coefficients were experimentally identified by the proposed method. The dimensionless parameters ϵ and r_{st} were translated to the dimensional running speed v and lateral steady-state amplitude y_{amp} . Figure 10 shows the comparison. The theoretical diagram obtained from the normal form with the experimentally identified coefficients is described with solid and dashed lines. The plots are the amplitudes directly obtained from the time histories of the experiments. There is a zero-amplitude solution below the linear critical speed in the theoretical result. However, in the experimental results, there is no zero steady-state amplitude due to the roughness of the roller rig. When increasing the running speed, we can regard the speed at which the amplitude increases abruptly as a Hopf bifurcation point. Also, when the running speed decreases, we can regard the speed at which the amplitude abruptly decreases as a saddle-node bifurcation point. Under these considerations, we conclude that the theoretical bifurcation diagram based on the normal form can qualitatively and quantitatively describe the characteristics of the quintic hunting motion. Therefore, the normal form with coefficients experimentally identified from the response amplitude at four different running speeds is a powerful tool for analyzing nonlinear hunting motion.

4 Conclusions

In this study, we used a roller rig, which has been used for experiments on the linear characteristics of hunt-

ing motion, to investigate the nonlinear characteristics of hunting motion. Knowledge of nonlinear hunting motion may increase running stability and ride comfort in railway vehicles. The experimentally observed results show the hysteresis and indicate the existence of subcritical Hopf and saddle-node bifurcations due to cubic and quintic nonlinear effects. We obtained the normal form, which can reflect characteristics of nonlinear hunting motion, using the center manifold theory. The number of nonlinear dimensionless coefficients governing the original equations is 20, but the number of nonlinear dimensionless coefficients in the normal form is 4. This indicates that these four coefficients are the essential parameters for capturing the nonlinear characteristics of the hunting motion.

Next, we proposed an identification method for these four coefficients using the experimentally observed bifurcation diagram. Comparison of the theoretically obtained and experimentally observed bifurcation diagrams showed that they are consistent, verifying the proposed identification method for the essential coefficients in the normal form.

Compliance with ethical standards

Conflict of interest The authors declare that they have no conflict of interest.

Appendix A: Hysteresis width depending on the amount of surface roughness or disturbance

Disturbances created from surface roughness can change the linear and nonlinear critical speeds, that is, the width of the hysteresis region, as follows. Figure 11 is a schematic bifurcation diagram. In the hysteresis region, the unstable steady-state amplitude is the threshold determining whether the amplitude grows up to the stable nontrivial steady-state amplitude or decreases to the zero amplitude. Therefore, when the disturbance is small, as in Fig. 11a, where the disturbance is denoted by short thick arrows, the linear and nonlinear critical speeds, v_c and v_n , are approximately equal to those theoretically obtained values under the assumption of an infinitely small disturbance. At these critical speeds, the amplitude grows or decreases along the thin arrow.

In contrast, under a large disturbance, as in Fig. 11b, where the disturbance is denoted by long thick arrows, the linear and nonlinear critical speeds decrease and

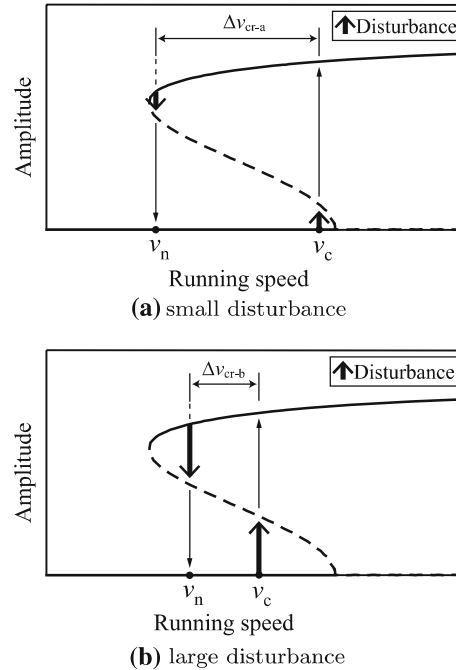


Fig. 11 Hysteresis width depending on the amount of surface roughness, that is, disturbance, in the roller rig. Δv_{cr} indicates the hysteresis width under different disturbance, where $\Delta v_{cr-a} > \Delta v_{cr-b}$. The solid and dashed curves denote the stable and unstable steady-state amplitudes, respectively

increase, respectively. Therefore, the threshold becomes narrower than it is for a small disturbance. As one application of these nonlinear characteristics, measurement of the width of threshold can prove an identical method for determining the amount of disturbance.

Appendix B: Eigenvalues of the equation of motion

Matrix A consists of the coefficients of the linear terms, and vector $N(\mathbf{x}, \epsilon)$ includes the cubic and quintic nonlinear terms and the detuning term denoted by the second term of Eq. (5). At the linear critical speed ($\epsilon = 0$), the four eigenvalues of the matrix A include a pair of pure imaginary eigenvalues as

$$\pm i\omega = \pm i\sqrt{\frac{d_{11}k_{22} + d_{22}k_{11}}{d_{11} + d_{22}}}, \quad (B-1)$$

and one complex conjugate pair of eigenvalues with a negative real part as

$$\lambda_R \pm i\lambda_I = -\frac{1}{2}C \pm \frac{1}{2}i\sqrt{4D - C^2}, \quad (\text{B-2})$$

where

$$\begin{aligned} C &= \frac{d_{11} + d_{22}}{v_c^*}, \\ D &= \frac{d_{11}d_{22}}{v_c^{*2}} + \frac{k_{11}d_{11} + k_{22}d_{22}}{d_{11} + d_{22}}. \end{aligned} \quad (\text{B-3})$$

Appendix C: Reduction in nonlinear terms of the equation of r

We obtain the equation governing η under the consideration of different orders from Eq. (21). The linear part ($O(\epsilon^{1/2})$) of Eq. (21) is obtained as:

$$\dot{\eta} = i\omega\eta, \quad (\text{C-1})$$

and the cubic part ($O(\epsilon^{3/2})$) of Eq. (21) is obtained as

$$\begin{aligned} \dot{\eta} &= i\omega\eta + \hat{N}_1(O(\eta^3)) + \frac{\partial q}{\partial \eta}(-i\omega\eta) + \frac{\partial q}{\partial \bar{\eta}}(i\omega\bar{\eta}) \\ &= D_1\epsilon\eta + (D_2 + 2i\omega\Gamma_2)\epsilon\bar{\eta} + (D_3 - 2i\omega\Gamma_3)\eta^3 \\ &\quad + D_4\eta^2\bar{\eta} + (D_5 + 2i\omega\Gamma_5)\eta\bar{\eta}^2 + (D_6 + 4i\omega\Gamma_6)\bar{\eta}^3. \end{aligned} \quad (\text{C-2})$$

To reduce the number of nonlinear terms in the equation, we consider

$$\begin{aligned} (D_2 + 2i\omega\Gamma_2)\epsilon\bar{\eta} &= 0, (D_3 - 2i\omega\Gamma_3)\eta^3 = 0, \\ (D_5 + 2i\omega\Gamma_5)\eta\bar{\eta}^2 &= 0, (D_6 + 4i\omega\Gamma_6)\bar{\eta}^3 = 0. \end{aligned} \quad (\text{C-3})$$

Therefore, the cubic nonlinear coefficients of Eq. (20) are selected as

$$\Gamma_2 = -\frac{D_2}{2i\omega}, \Gamma_3 = \frac{D_3}{2i\omega}, \Gamma_5 = -\frac{D_5}{2i\omega}, \Gamma_6 = -\frac{D_6}{4i\omega}, \quad (\text{C-4})$$

and we select Γ_1, Γ_4 as

$$\Gamma_1 = 0, \Gamma_4 = 0. \quad (\text{C-5})$$

Then, Eq. (C-2) is simplified as follows:

$$\dot{\eta} = D_1\epsilon\eta + D_4\eta^2\bar{\eta}. \quad (\text{C-6})$$

The quintic part ($O(\epsilon^{5/2})$) of Eq. (21) is obtained as follows:

$$\begin{aligned} \dot{\eta} &= i\omega\eta - (i\omega\eta + D_1\epsilon\eta + D_4\eta^2\bar{\eta})\frac{\partial q}{\partial \eta} \\ &\quad + (-i\omega\bar{\eta} + \bar{D}_1\epsilon\bar{\eta} + \bar{D}_4\eta\bar{\eta}^2)\frac{\partial q}{\partial \bar{\eta}} + \hat{N}_1(O(\eta^5)) \\ &= (D_7 + D_2\bar{\Gamma}_2)\epsilon^2\eta + (2i\omega\Gamma_8 + D_8 + D_1\Gamma_2 - \bar{D}_1\Gamma_2)\epsilon^2\bar{\eta} \\ &\quad + (-2i\omega\Gamma_9 + D_9 - 2D_1\Gamma_3 + D_2\bar{\Gamma}_6 + D_4\bar{\Gamma}_2)\epsilon\eta^3 \\ &\quad + (D_{10} + D_2\bar{\Gamma}_5 + 3D_3\Gamma_2 + 2D_5\bar{\Gamma}_2)\epsilon\eta^2\bar{\eta} \\ &\quad + (2i\omega\Gamma_{11} + D_{11} - 2\bar{D}_1\Gamma_5 - \bar{D}_4\Gamma_2 + 2D_4\Gamma_2 + 3D_6\bar{\Gamma}_2) \\ &\quad \epsilon\eta\bar{\eta}^2 \\ &\quad + (4i\omega\Gamma_{12} + D_{12} - 3\bar{D}_1\Gamma_6 + D_1\Gamma_6 + D_2\bar{\Gamma}_3)\epsilon\bar{\eta}^3 \\ &\quad + (-4i\omega\Gamma_{13} + D_{13} + 3D_3\Gamma_3 + D_4\bar{\Gamma}_6)\eta^5 \\ &\quad + (-2i\omega\Gamma_{14} + D_{14} - D_4\Gamma_3 + D_4\bar{\Gamma}_5 + 2D_5\bar{\Gamma}_6)\eta^4\bar{\eta} \\ &\quad + (D_{15} + 3D_3\Gamma_5 - D_5\bar{\Gamma}_6 + 2D_5\bar{\Gamma}_5 + 3D_6\bar{\Gamma}_6)\eta^3\bar{\eta}^2 \\ &\quad + (2i\omega\Gamma_{16} + D_{16} + D_4\Gamma_5 - 2\bar{D}_4\Gamma + 3D_3\Gamma_6 + D_4\bar{\Gamma}_3 \\ &\quad + D_5\bar{\Gamma}_5 + 2D_5\Gamma_5 + 3D_6\bar{\Gamma}_5)\eta^2\bar{\eta}^3 \\ &\quad + (4i\omega\Gamma_{17} + D_{17} - 3\bar{D}_4\Gamma_6 + 2D_4\Gamma_6 + 2D_5\bar{\Gamma}_3)\eta\bar{\eta}^4 \\ &\quad + (6i\omega\Gamma_{18} + D_{18} + D_5\bar{\Gamma}_3 + 3D_6\bar{\Gamma}_3)\bar{\eta}^5. \end{aligned} \quad (\text{C-7})$$

We consider that

$$\begin{aligned} (2i\omega\Gamma_8 + D_8 + D_1\Gamma_2 - \bar{D}_1\Gamma_2)\epsilon^2\bar{\eta} &= 0, \\ (-2i\omega\Gamma_9 + D_9 - 2D_1\Gamma_3 + D_2\bar{\Gamma}_6 + D_4\bar{\Gamma}_2)\epsilon\eta^3 &= 0, \\ (2i\omega\Gamma_{11} + D_{11} - 2\bar{D}_1\Gamma_5 - \bar{D}_4\Gamma_2 + 2D_4\Gamma_2 + 3D_6\bar{\Gamma}_2) \\ &\quad \epsilon\eta\bar{\eta}^2 = 0, \\ (4i\omega\Gamma_{12} + D_{12} - 3\bar{D}_1\Gamma_6 + D_1\Gamma_6 + D_2\bar{\Gamma}_3)\epsilon\bar{\eta}^3 &= 0, \\ (-4i\omega\Gamma_{13} + D_{13} + 3D_3\Gamma_3 + D_4\bar{\Gamma}_6)\eta^5 &= 0, \\ (-2i\omega\Gamma_{14} + D_{14} - D_4\Gamma_3 + D_4\bar{\Gamma}_5 + 2D_5\bar{\Gamma}_6)\eta^4\bar{\eta} &= 0, \\ (2i\omega\Gamma_{16} + D_{16} + D_4\Gamma_5 - 2\bar{D}_4\Gamma + 3D_3\Gamma_6 + D_4\bar{\Gamma}_3 \\ &\quad + D_5\bar{\Gamma}_5 + 2D_5\Gamma_5 + 3D_6\bar{\Gamma}_5)\eta^2\bar{\eta}^3 &= 0, \\ (4i\omega\Gamma_{17} + D_{17} - 3\bar{D}_4\Gamma_6 + 2D_4\Gamma_6 + 2D_5\bar{\Gamma}_3)\eta\bar{\eta}^4 &= 0, \\ (6i\omega\Gamma_{18} + D_{18} + D_5\bar{\Gamma}_3 + 3D_6\bar{\Gamma}_3)\bar{\eta}^5 &= 0. \end{aligned} \quad (\text{C-8})$$

Therefore, the quintic nonlinear coefficients of Eq. (20) are selected as

$$\begin{aligned} \Gamma_8 &= -(D_8 + D_1\Gamma_2 - \bar{D}_1\Gamma_2)/(2i\omega), \\ \Gamma_9 &= (D_9 - 2D_1\Gamma_3 + D_2\bar{\Gamma}_6 + D_4\bar{\Gamma}_2)/(2i\omega), \\ \Gamma_{11} &= -(D_{11} - 2\bar{D}_1\Gamma_5 - \bar{D}_4\Gamma_2 + 2D_4\Gamma_2 + 3D_6\bar{\Gamma}_2)/(2i\omega), \\ \Gamma_{12} &= -(D_{12} - 3\bar{D}_1\Gamma_6 + D_1\Gamma_6 + D_2\bar{\Gamma}_3)/(4i\omega), \\ \Gamma_{13} &= (D_{13} + 3D_3\Gamma_3 + D_4\bar{\Gamma}_6)/(4i\omega), \end{aligned}$$

$$\begin{aligned}\Gamma_{14} &= (D_{14} - D_4\Gamma_3 + D_4\bar{\Gamma}_5 + 2D_5\bar{\Gamma}_6)/(2i\omega), \\ \Gamma_{16} &= -(D_{16} + D_4\Gamma_3 - 2\bar{D}_4\Gamma + 3D_3\Gamma_6 + D_4\bar{\Gamma}_3 \\ &\quad + D_5\bar{\Gamma}_5 + 2D_5\Gamma_5 + 3D_6\bar{\Gamma}_5)/(2i\omega), \\ \Gamma_{17} &= -(D_{17} - 3\bar{D}_4\Gamma_6 + 2D_4\Gamma_6 + 2D_5\bar{\Gamma}_3)/(4i\omega), \\ \Gamma_{18} &= -(D_{18} + D_5\bar{\Gamma}_3 + 3D_6\bar{\Gamma}_3)/(6i\omega).\end{aligned}\quad (\text{C-9})$$

Then, we select Γ_7 , Γ_{10} , and Γ_{15} as

$$\Gamma_7 = 0, \Gamma_{10} = 0, \Gamma_{15} = 0. \quad (\text{C-10})$$

Finally, Eq. (C-7) is simplified:

$$\dot{\eta} = \Gamma'_7\epsilon^2\eta + \Gamma'_{10}\epsilon\eta^2\bar{\eta} + \Gamma'_{15}\eta^3\bar{\eta}^2, \quad (\text{C-11})$$

where

$$\begin{aligned}\Gamma'_7 &= D_7 + D_2\bar{\Gamma}_2, \quad \Gamma'_{10} = D_{10} + D_2\bar{\Gamma}_5 + 3D_3\Gamma_2 + 2D_5\bar{\Gamma}_2, \\ \Gamma'_{15} &= D_{15} + 3D_3\Gamma_5 + D_5\bar{\Gamma}_6 + 2D_5\bar{\Gamma}_5 + 3D_6\bar{\Gamma}_6.\end{aligned}\quad (\text{C-12})$$

Therefore, the equation of η in consideration of quintic nonlinearity ($O(\epsilon^{5/2})$) can be obtained as follows:

$$\begin{aligned}\dot{\eta} &= i\omega\eta + D_1\epsilon\eta + D_4\eta^2\bar{\eta} \\ &\quad + \Gamma'_7\epsilon^2\eta + \Gamma'_{10}\epsilon\eta^2\bar{\eta} + \Gamma'_{15}\eta^3\bar{\eta}^2.\end{aligned}\quad (\text{C-13})$$

References

1. Knothe, K., Bohm, F.: History of stability of railway and road vehicles. *Veh. Syst. Dyn.* **31**, 283–323 (1999)
2. Jin, X.S.: Key problems faced in high-speed train operation. *Appl. Phys. Eng.* **15**, 936–945 (2014)
3. Dai, J., Ang, K.K., Jiang, D.: Moving element analysis of high-speed rail system accounting for hanging sleepers. In: MATEC Web of Conferences. <https://doi.org/10.1051/matecconf/201814805007> (2018)
4. Han, L., Jing, L., Zhao, L.: Finite element analysis of the wheel-rail impact behavior induced by a wheel flat for high-speed trains: the influence of strain rate. Part FJ. *Rail Rapid Transit* **232**, 990–1004 (2018)
5. Law, E.H., Cooperrider, N.K.: A survey of railway vehicle dynamics research. *Dyn. Syst.* **96**, 132–146 (1974)
6. Wickens, A.H.: The dynamic stability of railway vehicle wheelsets and bogies having profiled wheels. *Int. J. Solids Struct.* **1**, 319–341 (1965)
7. Wickens, A.H.: Steering and dynamic stability of railway vehicles. *Veh. Syst. Dyn.* **5**, 15–46 (1976)
8. Wickens, A.H.: The dynamics of railway vehicles on straight track: fundamental considerations of lateral stability. In: Proceedings of the Institution of Mechanical Engineers, Conference Proceedings, vol. **180**, pp. 29–44 (1965)
9. Doyle, G.R., Prause, R.H.: Hunting stability of rail vehicles with torsionally flexible wheelsets. *J. Eng. Ind.* **99**, 10–17 (1977)
10. Lee, S., Cheng, Y.: Hunting stability analysis of high-speed railway vehicle trucks on tangent tracks. *J. Sound Vib.* **282**, 881–898 (2005)
11. Chi, M., Zhang, W., Zeng, J., Jin, X., Zhu, M.: Influence of hunting motion on ride quality of railway vehicle. *J. Vib. Eng.* **21**, 639–643 (2008)
12. Baldovin, D., Sireteanu, T., Simona, N., Mitu, A.M.: Dissipation effect in the hunting motion stability of wheel set with elastic joints. *Universitatea gEftimie Murguh Resita* **17**, 167–176 (2010)
13. Yabuno, H., Okamoto, T., Aoshima, N.: Effect of lateral linear stiffness on nonlinear characteristics of hunting motion of a railway wheelset. *Meccanica* **37**, 555–568 (2002)
14. Kaiser, I., Polach, O.: Comparison of methods analyzing bifurcation and hunting of complex rail vehicle models. *Comput. Nonlinear Dyn.* (2012). <https://doi.org/10.1115/1.4006825>
15. He, X.: Hopf bifurcation at infinity with discontinuous nonlinearities. *ANZIAM J.* **33**, 133–148 (1991)
16. Sakamoto, H., Yamamoto, M.: Effect of nonlinear creep force on railway truck dynamics. *Bull. JSME* **29**, 3102–3108 (1986)
17. Ahmadian, M., Yang, S.: Hopf bifurcation and hunting behavior in a rail wheelset with flange contact. *Nonlinear Dyn.* **15**, 15–30 (1998)
18. Hamid, M.S., Kourosh, H.S.: A survey of Hopf bifurcation analysis in nonlinear railway wheelset dynamics. *J. Vibro-eng.* **14**, 334–351 (2012)
19. Yokose, K., Igarashi, M.: Fundamental study on truck hunting considering non-linearity of creep force. *Bull. JSME* **29**, 541–547 (1986)
20. Banerjee, N., Karmakar, R.: Modelling of a free rail wheelset using non-linear creep force. *IJHVS* **21**, 310–327 (2014)
21. Guckenheimer J., Holmes P.: Local bifurcations. In: *Nonlinear Oscillations, Dynamical Systems, and Bifurcations of Vector Fields*. Applied Mathematical Sciences, vol 42, chap. 3. Springer, New York, NY (1983). https://doi.org/10.1007/978-1-4612-1140-2_3
22. Cheng, L., Wei, X., Cao, H.: Two-parameter bifurcation analysis of limit cycles of a simplified railway wheelset model. *Nonlinear Dyn.* **93**, 2415–2431 (2018)
23. Kim, P., Jung, J., Seok, J.: A parametric dynamic study on hunting stability of full dual-bogie railway vehicle. *Int. J. Precis. Eng. Manuf.* **12**, 505–519 (2011)
24. Hamid, M.S., Kourosh, H.S.: Bifurcation analysis in hunting dynamical behavior in a railway bogie: using novel exact equivalent functions for discontinuous nonlinearities. *Sci. Iran.* **19**, 1493–1501 (2012)
25. Zhang, T., Dai, H.: Loss of stability of a railway wheel-set, subcritical or supercritical. *Veh. Syst. Dyn.* **55**, 1731–1747 (2017)
26. Kim, P., Seok, J.: Bifurcation analysis on the hunting behavior of a dual-bogie railway vehicle using the method of multiple scales. *J. Sound Vib.* **329**, 4017–4039 (2010)
27. Zhang, B., Zeng, J., Liu, W.: Research on stochastic stability and stochastic bifurcation of suspended wheelset. *J. Mech. Sci. Technol.* **29**, 3097–3107 (2015)

28. Uyulan, G., Gokasan, M., Bogosyan, S.: Dynamic investigation of the hunting motion of a railway bogie in a curved track via bifurcation analysis. *Math. Probl. Eng.* **1**, 1–15 (2017)
29. Zboinski, K., Dusza, M.: Self-exciting vibrations and Hopf's bifurcation in non-linear stability analysis of rail vehicles in a curved track. *Eur. J. Mech.* **29**, 190–203 (2010)
30. Von Wagner, U.: Nonlinear dynamic behavior of a railway wheelset. *Veh. Syst. Dyn.* **47**, 627–640 (2009)
31. Chi, M., Wu, X.: Parameters study of Hopf bifurcation in railway vehicle system. *Comput. Nonlinear Dyn.* (2015). <https://doi.org/10.1115/1.4027683>
32. Yamanaga, Y., Kido, K.: Hunting stability test of railway bogies on roller rigs and bifurcation. In: Dynamics and Design Conference. https://doi.org/10.1299/jsmedmc.2017_304 (2017)
33. Dong, H., Zeng, J., Xie, J., Jia, L.: Bifurcation/instability forms of high speed railway vehicles. *Sci. China Technol. Sci.* **56**, 1685–1696 (2013)
34. Jaschinski, A., Chollet, H., Iwnicki, S.D., Wickens, A.H., Von Wurzen, J.: The application of the roller rigs to railway vehicle dynamics. *Veh. Syst. Dyn.* **31**, 345–392 (1999)
35. Ejiri, K., Michitsuji, Y., Suda, Y., Lin, S., Sugiyama, H.: Running stability analysis of independently rotating wheelset with negative tread conicity using scaled-model roller rig. *JSME* **79**, 4950–4962 (2013)
36. Myamlin, S., Kalivoda, J., Neduzha, L.: Testing of railway vehicles using roller rigs. *Procedia Eng.* **187**, 688–695 (2017)
37. Iwnicki, S.D., Wickens, A.H.: Validation of a Matlab railway vehicle simulation using a scale roller rig. *Veh. Syst. Dyn.* **30**, 257–270 (1998)
38. Yamanaga, Y., Watanabe, N.: Experimental investigation of global stability against hunting oscillation using a real bogie. *Trans. JSME (The Japanese Journal of Educational Research)* **84**, 18–00109 (2018)
39. Nayfeh, A.H.: The Method of Normal Forms. Wiley, Hoboken (2011)
40. Pirbodaghi, T., Hoseini, S.H., Ahmadian, M.T., Farrahi, G.H.: Duffing equations with cubic and quintic nonlinearities. *Comput. Math. Appl.* **57**, 500–506 (2009)
41. Iwnicki, S.D.: Handbook of Railway Vehicle Dynamics. Taylor and Francis, Didcot (2006)
42. Nana, B., Yamgoue, S.B., Tchitnga, R., Woaf, P.: Nonlinear dynamics of a sinusoidally driven lever in repulsive magnetic fields. *Nonlinear Dyn.* **91**, 55–66 (2018)
43. Kwuimy, C.K., Woaf, P.: Experimental realization and simulations a self-sustained macro electromechanical system. *Mech. Res. Commun.* **37**, 106–110 (2010)
44. De Pater, A.D.: The exact theory of the motion of a single wheelset on a perfectly straight track. *Veh. Syst. Dyn.* **8**, 182–184 (1979)
45. True, H.: Dynamics of a rolling wheelset. *Appl. Mech. Rev.* **46**, 438–444 (1993)
46. Knudsen, C., Feldberg, R., True, H.: Bifurcations and chaos in a model of a rolling railway wheelset. *Philos. Trans. R. Soc. Lond. A* **338**, 455–469 (1992)
47. Zhang, T., Dai, H.: Bifurcation analysis of high-speed railway wheel-set. *Nonlinear Dyn.* **83**, 1511–1528 (2016)
48. Steiner, W., Steinidl, A., Troger, H.: Center manifold approach to the control of a tethered satellite system. *Appl. Math. Comput.* **70**, 315–327 (1995)

Publisher's Note Springer Nature remains neutral with regard to jurisdictional claims in published maps and institutional affiliations.